AGU PUBLICATIONS

Paleoceanography

RESEARCH ARTICLE
10.1002/2013PA002553

Key Points:
- High-resolution record of Nile discharge from foraminiferal oxygen isotopes
- Early-Holocene Nile dominated by Indian Ocean moisture
- Solar cycles in Mediterranean sapropel S1 intensity linked to Nile discharge

Correspondence to:
R. Hennekam,
f.m.hennekam@uu.nl

Citation:
Hennekam, R., T. Jilbert, B. Schnetger, and G. J. de Lange (2014), Solar forcing of Nile discharge and sapropel S1 formation in the early to middle Holocene eastern Mediterranean, *Paleoceanography*, *29*, 343–356, doi:10.1002/2013PA002553.

Received 22 AUG 2013
Accepted 11 APR 2014
Accepted article online 15 APR 2014
Published online 19 MAY 2014

Solar forcing of Nile discharge and sapropel S1 formation in the early to middle Holocene eastern Mediterranean

Rick Hennekam[1], Tom Jilbert[1], Bernhard Schnetger[2], and Gert J. de Lange[1]

[1]Department of Earth Sciences-Geochemistry, Faculty of Geosciences, Utrecht University, Utrecht, Netherlands, [2]Institute of Chemistry and Biology of the Marine Environment, Carl von Ossietzky University, Oldenburg, Germany

Abstract We present high-resolution records for oxygen isotopes of the planktic foraminifer *Globigerinoides ruber* ($\delta^{18}O_{ruber}$) and bulk sediment inorganic geochemistry for Holocene-age sediments from the southeast Mediterranean. Our $\delta^{18}O_{ruber}$ record appears to be dominated by Nile discharge rather than basin-scale salinity/temperature changes. Nile discharge was enhanced in the early to middle Holocene relative to today. The timing of the long-term maximum in Nile discharge during the early Holocene corresponds to the timing of maximum intensity of the Indian Ocean-influenced Southwest Indian summer monsoon (SIM). This coincidence suggests a major influence of an Indian Ocean moisture source on Nile discharge in the early to middle Holocene, while, presently, the Atlantic Ocean is the main moisture source. Nile discharge was highly variable on multicentennial time scale during the early to middle Holocene, being strongly influenced by variable solar activity. This solar-driven variability is also recorded in contemporaneous SIM records, however, not observed in an Atlantic Ocean-derived West African summer monsoon record from the Holocene. This supports the hypothesis that the Indian Ocean moisture source predominantly controlled Nile discharge at that time. Solar-driven variability in Nile discharge also influenced paleoenvironmental conditions in the eastern Mediterranean. Bulk sediment Ba/Al and V/Al, used as indicators for (export) productivity and redox conditions, respectively, varied both in response to solar forcing on multicentennial time scales. We suggest that changes in Nile discharge on these time scales have been concordant with nutrient inputs to, and shallow ventilation of, the eastern Mediterranean.

1. Introduction

The discharge (rate of outflow) of the River Nile into the Mediterranean Sea is mainly dependent on changes in the intensity and northward penetration of the monsoonal rainbelt associated with the Intertropical Convergence Zone (ITCZ) [*Nicholson*, 2009]. Nile discharge can therefore be seen as a gauge, detecting the amount of precipitation falling in the Nile catchment due to the northeast African monsoon. The persistence of Nile outflow throughout contrasting climatic regimes of the late Pleistocene and Holocene epochs means that reconstructions of Nile discharge may contain invaluable paleoenvironmental information. For example, variability in the relative contribution of the two main moisture sources contributing to Nile outflow—the Atlantic Ocean and the Indian Ocean [*Mohamed et al*., 2005]—may be expected to influence Nile discharge. Understanding how such large-scale hydrological patterns respond to external forcing factors such as Milankovitch cycles is a key goal of climate science. Moreover, the continuity of Nile outflow potentially facilitates reconstructions of short time scale (i.e., sub-Milankovitch) climatic variability, provided that the climatic archives used to reconstruct Nile discharge are of adequately high resolution.

At present most of the Nile outflow (~70%) derives from the Blue Nile/Atbara Rivers (Figure 1a) [*Foucault and Stanley*, 1989]. These rivers originate from the Ethiopian Highlands, have a mainly Atlantic-derived moisture source, and have their peak outflow around August [*Mohamed et al*., 2005]. The remaining ~30% of Nile outflow derives from the White Nile. This originates from the Equatorial African mountain ranges (Figure 1a; most notably Lake Victoria), has a mixed Atlantic/Indian Ocean origin, and maintains the perennial flow into the main Nile [*Mohamed et al*., 2005]. In contrast, during the early to middle Holocene, large-scale moisture patterns were rearranged in response to the orbital precession cycle, meaning that Indian Ocean-derived moisture had an increased influence on Nile outflow [*Hamann et al*., 2009]. However, it has not yet been investigated to what extent the enhanced Indian Ocean moisture source influenced sub-Milankovitch time scale variability in Nile discharge during that time.

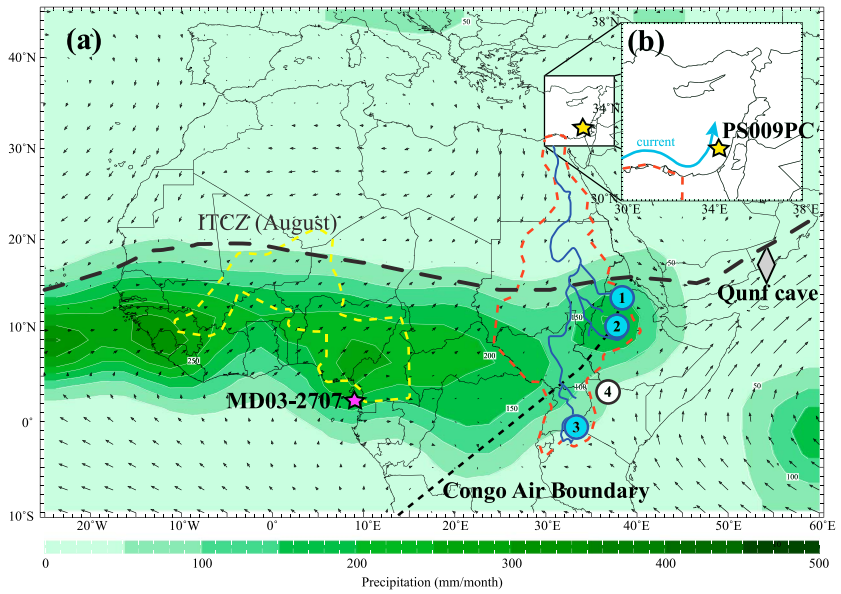

Figure 1. Overview of environmental setting and sites used in this study. (a) August wind field (925 hPa; small black arrows) and precipitation intensity (green shading) over northern Africa (http://iridl.ldeo.columbia.edu). The ITCZ position and the Congo Air Boundary (zone of confluence between Atlantic- and Indian Ocean-derived moisture [*Tierney et al*., 2011]) (black dashed lines), the Niger/Sanaga catchment (yellow dashed line), and the Nile catchment area (orange dashed line) are indicated. Numbers indicate (1) Atbara River, (2) Blue Nile River, (3) White Nile River, and (4) Lake Turkana. Sites: PS009PC (yellow star; this study), MD03-2707 (purple star) [*Weldeab et al*., 2007], and Qunf Cave (grey diamond) [*Fleitmann et al*., 2003]. (b) Eastern Mediterranean with core PS009PC (32°07.7′N, 34°24.4′E; 552 m water depth). The primary current direction is indicated with a blue arrow.

This study focuses on a marine sediment core (PS009PC) from the southeast Levantine Basin (Figure 1b). This area is known to be largely influenced by Nile sedimentation [*Krom et al*., 1999] and to have maintained high sedimentation rates throughout the Holocene [*Schilman et al*., 2001; *Almogi-Labin et al*., 2009; *Hamann et al*., 2009; *Castañeda et al*., 2010; *Box et al*., 2011]. Variability in Nile River discharge is, consequently, documented at this core location by indicators of the freshwater input (such as planktic foraminifer oxygen isotopes) and bulk sediment composition [*Fontugne et al*., 1994; *Almogi-Labin et al*., 2009]. Moreover, the high sedimentation rates (12.5–104 cm kyr^{-1}) and high sampling resolution (0.5 cm, thus ≤ 40 year per sample) allow the identification of centennial variability in Nile outflow. Hence, for the first time, we report on the sub-Milankovitch variability in Nile discharge during the early to middle Holocene.

The sediment core used in this study is considered not only to be a high-resolution archive of northeast African climate but also to be an indicator for the paleoenvironment of the eastern Mediterranean [e.g., *Almogi-Labin et al*., 2009]. The sensitivity of the eastern Mediterranean to the northeast African climate is demonstrated by the intermittent deposition of distinct organic-rich sediment layers (sapropels). Periods of increased Nile discharge have been closely associated to sapropel formation in the eastern Mediterranean [*Rossignol-Strick et al*., 1982]. These periods of increased Nile outflow are generally thought to be due to precession-forced insolation changes causing increased monsoonal activity. The increased Nile discharge, subsequently, may have influenced ventilation and/or productivity in the eastern Mediterranean, thus promoting sapropel deposition [e.g., *Rossignol-Strick et al*., 1982; *Rohling and Hilgen*, 1991; *Rohling*, 1994; *Thomson et al*., 1999; *De Lange et al*., 2008]. The high sedimentation rate site of this study permits us to evaluate at high resolution the paleoclimate-related mechanisms of, and variability within, sapropel formation and its link to Nile discharge.

2. The Core Locality and Oceanographic Setting

Piston core PS009PC (32°07.7′N, 34°24.4′E; 552 m water depth) and box core PS008BC (same coordinates) were taken during the PASSAP cruise with the R/V *Pelagia* in May 2000. This coring site is located in the southeast Levantine Basin, approximately 100 km southwest of Haifa, Israel (Figure 1b).

Table 1. The ^{14}C and ^{210}Pb Data Used to Construct the Age Model

Depth (cm)	^{14}C Age (year B.P.) $\pm 2\sigma$	Calendar Age (cal year B.P.) $\pm 2\sigma$	^{210}Pb Age (year B.P.) $\pm 2\sigma$	Final Age Model (year B.P.)	Material	^{14}C Lab Code
0	-	-	-25 ± 10	-25	Sediment	
8.75	-	-	69 ± 15	59	Sediment	
67.5	$1{,}690 \pm 30$	$1{,}205 \pm 146$	-	1,111	*G. ruber*, *G. sacculifer*, and *O. universa*	Poz-40169
132.1	$3{,}320 \pm 30$	$3{,}138 \pm 193$	-	3,240	*G. ruber*, *G. sacculifer*, and *O. universa*	Poz-40170
191.2	$5{,}750 \pm 40$	$6{,}118 \pm 169$	-	6,080	*G. ruber* and *G. sacculifer*	Poz-40171
217.2	$7{,}950 \pm 40$	$8{,}388 \pm 166$	-	8,155	*G. ruber*	Poz-40173
247.2	$9{,}620 \pm 50$	$10{,}433 \pm 186$	-	10,548	*G. ruber* and *G. sacculifer*	Poz-40174
285.2	$12{,}000 \pm 60$	$13{,}460 \pm 204$	-	13,580	*G. ruber*, *G. sacculifer*, and *O. universa*	Poz-40175
322.6	$13{,}950 \pm 80$	$16{,}581 \pm 374$	-	16,565	*G. ruber* and *G. sacculifer*	Poz-40176

Mediterranean surface water (MSW), originating from the Atlantic, follows an eastward path through the eastern Mediterranean basin. On its way its salinity increases, because of excess evaporation, to values above 39 [*Wüst*, 1961]. In the eastern Mediterranean the MSW flows anticlockwise, being diverted northward in the southeast Levantine Basin along, respectively, the Israeli, Lebanese, and Syrian coastlines to southern Turkey [*Pinardi and Masetti*, 2000]. It is this current that transports much of the Nile sediment to our core location, resulting in high sedimentation rates (Figure 1b). Concurringly, the Nile freshwater input is diverted in the same direction. This is indicated by the occurrence of a distinct freshwater anomaly in the southeast Levantine Basin, which was observed prior to completion of the high Aswan Dam in 1964 [*Hecht and Gertman*, 2001]. West of Cyprus, in the Rhodes gyre, Levantine Intermediate Water (LIW) is formed during intense winter cooling of already saline MSW by relatively cold northern air masses [*Lascaratos et al.*, 1993]. This LIW flows to depths between 200 and 600 m and spreads over the entire Mediterranean basin [*Wüst*, 1961]. Subsequently, Eastern Mediterranean Deep Water (EMDW), flowing below depths of 1500 m [*Wüst*, 1961], is formed in the southern Adriatic basin [*Schlitzer et al.*, 1991] and (occasionally) in the southern Aegean basin [*Roether et al.*, 1996]. This happens in winter, due to mixing of LIW with relatively cold but less saline waters in those basins.

3. Material and Methods

3.1. Core Chronology

The age model for core PS009PC was constructed by means of 11 ^{210}Pb measurements on sediment samples of PS008BC and 7 ^{14}C accelerator mass spectrometry (AMS) measurements on planktonic foraminiferal samples of PS009PC (Table 1). Box core PS008BC was sampled every 0.5 cm for its full 34 cm length. The samples were freeze dried and ground to powder using an agate mortar. The ^{210}Pb activity was subsequently measured at the Royal Netherlands Institute for Sea Research (NIOZ) (Figure 2a), and a constant rate of supply (CRS) model was used to construct the age-depth profile (for details see *Boer et al.* [2006]) (Figure 2b). The correlation of PS008BC to PS009PC using elemental ratios was made in *Hennekam and De Lange* [2012]. By the use of two correlation points the ages of the top and 8.75 cm depth in PS009PC were determined, relating to, respectively, 1975 and 1881 year A.D. (Figure 2b).

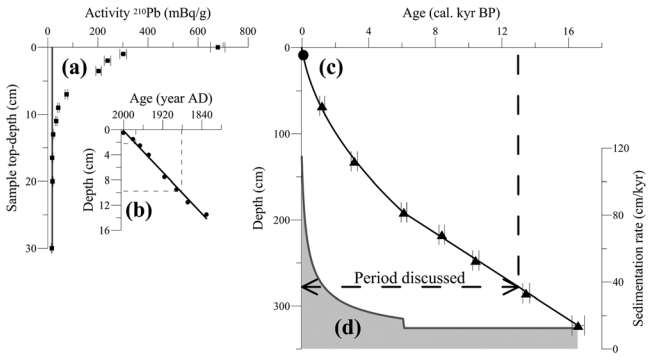

Figure 2. Age model of core PS009PC. (a) Depth profile of excess ^{210}Pb of box core PS008BC, including horizontal error bars. (b) Constant rate of supply (CRS) age model, based on ^{210}Pb data. Dashed lines indicate correlation points of PS008BC to PS009PC and corresponding ages. (c) Final age model based on seven calibrated ^{14}C ages (triangles; horizontal error bars are indicated) and correlation of PS009PC to PS008BC ^{210}Pb age model for the top (circle). (d) Sedimentation rate (grey line) through time, by using the final age model.

Table 2. Data Used to Deduce the Mass Accumulation Rates (MARs)[a]

Depth (cm)	Water (wt %)	Salt (wt %)	Sediment (wt %)	Porosity (vol %)	DBD (g/cm^3)	Sed. Rate (cm/kyr)	MAR ($g/cm^2/kyr$)
0	-	-	-	-	-	-	-
8.75	58.2	2.24	39.6	80.8	0.51	104	52.6
67.5	57.3	2.21	40.5	80.2	0.52	55.9	29.3
132.1	54.2	2.09	43.7	77.9	0.58	30.3	17.7
191.2	55.2	2.12	42.7	78.7	0.56	20.8	11.2
217.2	53.9	2.08	44.0	77.7	0.59	12.5	7.39
247.2	48.5	1.87	49.6	73.4	0.70	12.5	8.82
285.2	43.9	1.69	54.4	69.4	0.81	12.5	10.2
322.6	37.0	1.42	61.6	62.7	0.99	12.5	12.4

[a]A bottom water density of 1.027 g/cm^3 and a sediment density of 2.65 g/cm^3 were used to calculate porosity and dry bulk density (DBD).

The sediment samples for ^{14}C analysis were first wet sieved using deionized water over a 150 μm sieve. Per sample approximately 10 mg of a mixture of planktonic foraminiferal material was picked (Table 1). The ^{14}C analyses were done at the Poznań Radiocarbon Laboratory in Poland. For ^{14}C age conversion to calendar ages the OxCal 4.1.7 program was used [*Ramsey*, 2009]. The Marine'09 data set was used for calibration [*Reimer et al*., 2009] with a local reservoir correction (ΔR) of 21 ± 63 year. This reservoir correction was based on ^{14}C analyses of recent shell material near the core locality [*Reimer and McCormac*, 2002; *Boaretto et al*., 2010].

The final age model for the upper 190 cm was constructed using the uppermost four samples and a second-order polynomial best fit, with a fixed start at 1975 (i.e., −25 cal years B.P.) (Figure 2c). The change in sedimentation rate is a result not only of different water contents but also of a change in mass accumulation rates (MARs) (Table 2). The increased MAR to the top is thought to relate to gradually drier conditions in the Ethiopian Highlands, enhancing erosion [see *Box et al*., 2011]. A significant increase during the last ~2500 year B.P. might be related to extra soil erosion due to deforestation in the same region [*Darbyshire et al*., 2003]. A linear best fit was used to construct the age model of the samples from 191 to 323 cm, expressing the relatively constant sedimentation rates in this core segment (Figure 2d). The age at 191 cm was fixed to acquire a smooth flow from the top segment to the bottom segment of the age model.

Certain factors might influence the accuracy of age models based on foraminiferal ^{14}C measurements (i.e., measurement uncertainties, depositional events, bioturbation, and variable reservoir ages). Measurement uncertainties are inherent to the use of ^{14}C for dating and are in the order of several decades for these samples (Table 1). Event-related deposits are generally detectable in the sedimentological and geochemical composition of the sediment, but these were not detected in this core. The age effect of bioturbation on high sedimentation rate sites is limited [*Siani et al*., 2001], as is also indicated by a poorly developed top mixed layer in the ^{210}Pb activity profile of core PS008BC (Figure 2a). Moreover, during sapropel S1 formation, bioturbation was probably reduced by the low oxygen concentrations of the eastern Mediterranean bottom water. Understanding past variability in sea surface reservoir ages is crucial for a robust age model. For the eastern Mediterranean, sea surface reservoir ages during the Holocene remained similar to the midlatitudes of the Atlantic Ocean [*Siani et al*., 2001]. Therefore, we believe that calibration to the Marine'09 data set with a minor local reservoir correction is valid for our targeted time interval. Due to uncertainty within reservoir ages and tuning to the Marine'09 curve, the 2σ uncertainties of the calendar ages increase to ~150–200 years within the Holocene (Table 1). Nevertheless, the final age model concords well to the ^{14}C-based age models from similar locations [e.g., *Hamann et al*., 2008; *Castañeda et al*., 2010], showing relatively constant sedimentation rates during the early to middle Holocene and increasing sedimentation rates during the late Holocene.

As this study focuses on the Holocene, the samples in the time window 0–13 cal kyr B.P. were used for further analyses.

3.2. Geochemical Analysis

The top 278 cm (≈13 kyr) of core PS009PC was subsampled with a 0.5 cm resolution (average of ~23 year per sample) for geochemical analysis. The bulk inorganic analyses for Al, Ti, V, and Ba were made by X-ray

fluorescence using glass beads at the Institute of Chemistry and Biology of the Marine Environment in Oldenburg with a Philips PW 2400 X-ray spectrometer. An agate mortar was used for powdering and homogenizing of the freeze-dried samples. The samples (~700 mg per sample) were mixed with lithium tetraborate (4200 mg), preoxidized at 500°C with ammonium nitrate, and subsequently fused to glass beads, following the procedure of *Schnetger et al.* [2000]. The analytical accuracy and precision, as deduced from replicate analyses of international reference material and in-house standards, was better than 2% for Al and Ti and better than 6% for V and Ba.

Samples were analyzed for total organic carbon content (C_{org}) at 2.5 cm resolution (0.5 cm sample interval) for the depths from 0 to 185.5 cm (≈0–5.8 cal kyr B.P.) and 259.5–278 cm (≈11.5–13 cal. kyr B.P.). In the depth range 185.5–259.5 cm (≈5.8–11.5 cal. kyr B.P. ≈ "sapropel period"), all samples (0.5 cm resolution) were analyzed. The samples were decalcified using 1 M hydrogen chloride (for details see *Van Santvoort et al.* [1996]) and were subsequently measured with a Fisons-type NA 1500 NCS elemental analyzer. International reference material and replicate standards show a precision and accuracy of $<3\%$.

3.3. Globigerinoides Ruber Oxygen Isotope Analysis

Approximately half of the subsampled material (sampled at a 0.5 cm resolution) was used for oxygen isotope analyses on foraminifers, combining two consecutive samples, thus resulting in a 1 cm resolution. The foraminifer sediment samples were first washed with deionized water over a 63 μm and 150 μm sieve. The remaining fractions were then oven dried and dry sieved. Approximately 20–30 tests/sample of the sea surface dwelling foraminifer *Globigerinoides ruber* (white) were handpicked. To obtain a sufficient quantity of *G. ruber* tests for samples above 173 cm, a 212–300 μm size range was used. For samples deeper than 173 cm (≈5.1 cal kyr B.P.) a narrower size range of 250–300 μm was used.

To remove organic matter, the picked foraminifer tests were cleaned by the addition of ~10% hydrogen peroxide (H_2O_2) for 20 min, with a 2 s sonification after 10 min. The H_2O_2 was removed using a pipette, and the sample was flushed once with deionized water. Methanol (CH_3OH) was added, and after 10 s of sonification the liquid and fine-grained material was removed with a pipette. The tests were then rinsed again with deionized water and dried for at least 24 h in an active fume hood. The foraminifer tests were crushed and mixed, and an amount of 20–60 μg was weighed before putting it into the Kiel-III carbonate preparation device. After reaction of the carbonate with H_3PO_4, the stable isotope values were measured with a Finnigan MAT-253 mass spectrometer at the University of Utrecht. During the process, 137 measurements of the NBS-19 standard were done with a standard deviation of ±0.06‰ for $\delta^{18}O$. The oxygen isotope measurements are reported in per mil (‰) relative to the Vienna PeeDee belemnite.

3.4. Companion Records for Paleoenvironmental Reconstructions

In order to investigate the global climatic controls on the observed paleoenvironmental variability in the eastern Mediterranean, three globally relevant, high-resolution, paleoclimatic records were selected for comparison. The record of Ba/Ca in *G. ruber* tests from core MD03-2707 taken in the Gulf of Guinea (Figure 1a) [*Weldeab et al.*, 2007] has been reported to reflect hydrological conditions of the Atlantic Ocean-derived West African monsoon (WAM). Contrarily, the $\delta^{18}O_{speleothem}$ record from the Qunf Cave in Oman record has been suggested to represent the intensity of the Indian Ocean-derived Southwest Indian summer monsoon (SIM) (Figure 1a) [*Fleitmann et al.*, 2003]. Variations in solar output has been claimed to be one of the main drivers of multicentennial climatic variability in the Holocene [e.g., *Bond et al.*, 2001; *Fleitmann et al.*, 2003; *Wang et al.*, 2005]. The tree ring-based $\Delta^{14}C$ residual record ($\Delta^{14}C_{res}$) mainly reflects variability in the strength of the solar wind [*Stuiver and Braziunas*, 1993]. The $\Delta^{14}C_{res}$ record [*Stuiver et al.*, 1998] has, therefore, been used as a proxy for solar output intensity.

3.5. Data Processing and Wavelet Analysis

In order to focus on multicentennial time scale variability in selected time series, low-frequency variability in our data was removed by applying a notch filter ("band-stop"; *frequency* = 0.0 and band width = 0.3 kyr). The notch filter removed wavelengths >3.333 kyr. Filtering was done by using the AnalySeries program [*Paillard et al.*, 1996]. Furthermore, the proxy records were detrended, and the mean was subtracted for an optimal comparison between all records.

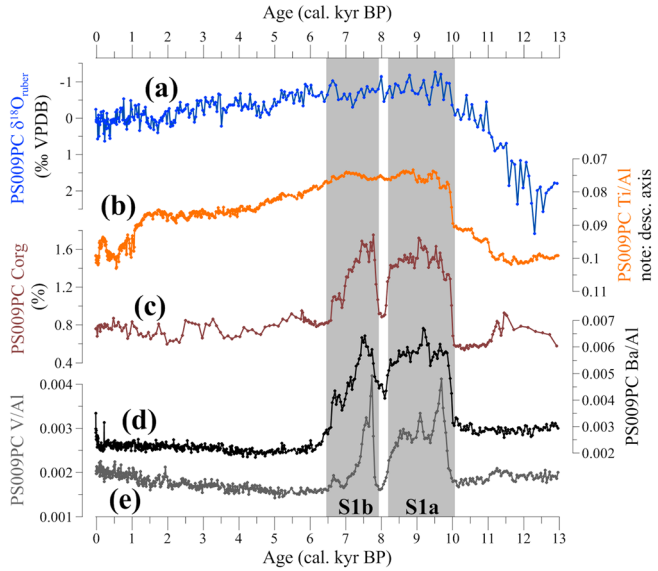

Figure 3. Data from core PS009PC (a) $\delta^{18}O_{ruber}$, (b) Ti/Al (note descending axis), (c) total organic carbon concentrations, (d) Ba/Al, and (e) V/Al. Grey-shaded areas indicate period of sapropel S1 formation, while S1a and S1b are also specified.

In order to explore the frequency variability over time, a continuous wavelet transform (CWT) was performed, using a Morlet wavelet, within the Paleontological Statistics software package [*Hammer et al.*, 2001]. Before analysis the proxy records were filtered, as detailed above, and resampled at a continuous and higher 1 year resolution to maintain all available frequency data within all proxy records.

The outcome of the CWT was used to select the window width (1005 years) for a running correlation procedure. Data points in the running correlation represent a linear correlation magnitude (Pearson's R) between two time series within a window of 1005 years centered at that specific data point. Running correlations, relative to the $\Delta^{14}C_{res}$ record [*Stuiver et al.*, 1998], were performed between the WAM record [*Weldeab et al.*, 2007], SIM record [*Fleitmann et al.*, 2003], and $\delta^{18}O_{ruber}$ (this study). We have focused on multicentennial variability by applying filtering as above and applying an additional low-pass filter with a cutoff at 256 years for smoothing (resulting in an overall band-pass filter of all records between 0.256 and 3.333 kyr) within the AnalySeries program [*Paillard et al.*, 1996].

4. Results

4.1. General Trends in the Holocene Proxy Records of PS009PC

The *G. ruber* oxygen isotope record from core PS009PC shows a shift from enriched $\delta^{18}O_{ruber}$ values (~2.5‰) around 12.5 cal kyr B.P. to a much more depleted $\delta^{18}O_{ruber}$ value of −1.26‰ at ~9.5 cal kyr B.P. (Figure 3a). Thereafter, the record shows a long-term trend from ~9.5 cal kyr B.P. to present of gradually more enriched values. The Ti/Al record of PS009PC shows a similar evolution to that of $\delta^{18}O_{ruber}$, with a rapid decrease from 12.5 cal kyr B.P. to 9.5 cal kyr B.P., followed by a gradual increase toward the present (Figure 3b).

The C_{org}, Ba/Al, and V/Al records are dominated by the presence of sapropel S1 from ~10.1–6.5 kyr B.P. (Figures 3c–3e), and therefore, their general trends contrast markedly with $\delta^{18}O_{ruber}$ and Ti/Al. The S1 interval shows high C_{org}, high Ba/Al, and high V/Al, with an interruption around ~8.2–7.9 cal kyr B.P. splitting the sapropel S1 into, respectively, "S1a" and "S1b" segments (Figures 3c–3e). The interruption displays C_{org} and V/Al similar to nonsapropel values. Ba/Al is also depleted in the interruption but remains elevated with respect to nonsapropel values.

4.2. Short–Time Scale Variability in the Holocene Proxy Records of PS009PC

Multicentennial variability is observed in the $\delta^{18}O_{ruber}$ record throughout the Holocene and in the C_{org}, Ba/Al, and V/Al records during sapropel S1 (Figures 3a and 3c–3e). During the S1 interval, many of the multicentennial features appear to be coincident for all proxies. Five negative $\delta^{18}O_{ruber}$ excursions, including one pronounced excursion at the onset of S1, are reproduced in the C_{org}, Ba/Al, and V/Al records (Figures 3a and 3c–3e). However, the clear midsapropel interruption observed in C_{org}, Ba/Al, and V/Al is accompanied by only a minor positive excursion in $\delta^{18}O_{ruber}$ (~0.3‰).

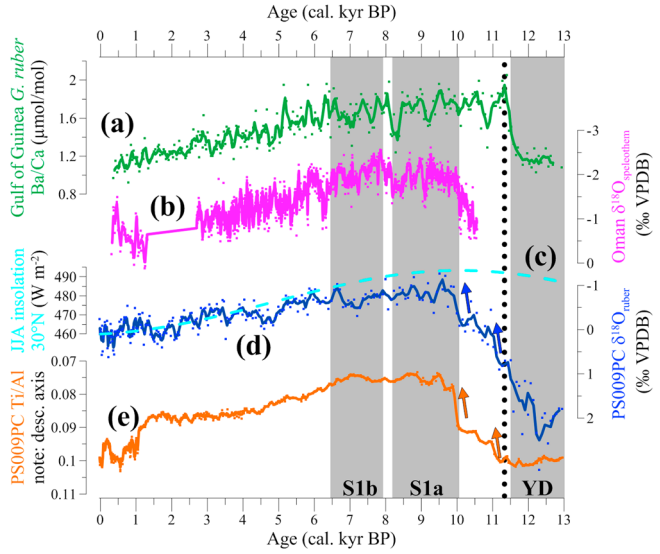

Figure 4. (a) Ba/Ca in *G. ruber* tests of core MD03-2707 in Gulf of Guinea (higher Ba/Ca values indicate stronger WAM) [*Weldeab et al.*, 2007]. (b) $\delta^{18}O_{speleothem}$ record from Qunf Cave, Oman (more depleted $\delta^{18}O_{speleothem}$ relate to a stronger SIM) [*Fleitmann et al.*, 2003]. (c) June-July-August insolation at 30°N [*Laskar et al.*, 2004]. (d) $\delta^{18}O_{ruber}$ of core PS009PC (this study). (e) Ti/Al of core PS009PC (note descending axis). All data are three-point moving averages. Grey-shaded areas indicate periods of Younger Dryas (YD) and sapropel S1 formation, while S1a and S1b are also specified (based on data from Figure 3). Vertical dotted line marks period of maximum WAM (based on *G. ruber* Ba/Ca of MD03-2707).

5. Discussion

5.1. Nile Discharge and Moisture Sources During the Early to Middle Holocene

G. ruber is abundantly found in core PS009PC throughout the Holocene. The modern day Mediterranean *G. ruber* has its peak abundance during the late summer around August. It prefers to live in the upper 50 m of the water column during summer and in the upper 100 m during winter [*Pujol and Grazzini*, 1995]. *G. ruber* is known for its resistance to freshwater disturbances, being one of the most euryhaline foraminifer species, capable to inhabit freshwater lenses [e.g., *Schmuker and Schiebel*, 2002]. The average yearly peak of Nile discharge is in August [*Williams et al.*, 2006, and references therein]. The basin-wide peak abundance of *G. ruber* thus appears to coincide with, but not to be directly related to, the peak of Nile discharge.

In general, the $\delta^{18}O$ of foraminiferal calcite is controlled by temperature-dependent isotopic fractionation between water and calcite and by the isotopic composition of seawater. The latter is influenced by ice volume, freshwater input, and evaporation/precipitation [e.g., *Rohling and Bigg*, 1998]. Alkenone-derived sea surface temperatures indicate relatively constant temperatures throughout the Holocene in the eastern Mediterranean [*Essallami et al.*, 2007; *Almogi-Labin et al.*, 2009; *Castañeda et al.*, 2010]. Typical eastern Mediterranean $\delta^{18}O_{ruber}$ records will, therefore, mainly document seawater $\delta^{18}O$ changes during the Holocene. The latter is influenced by the evaporation/precipitation budget and by major river systems. Earlier work has shown that the Holocene $\delta^{18}O_{ruber}$ records from our study area differ from typical eastern Mediterranean $\delta^{18}O_{ruber}$ data [*Fontugne and Calvert*, 1992; *Fontugne et al.*, 1994; *Almogi-Labin et al.*, 2009]. *Fontugne et al.* [1994] show that in the Israeli coastal area the $\delta^{18}O_{ruber}$ values are up to >1.3‰ more depleted during sapropel S1 formation and become progressively more enriched to the west. These authors indicate that Nile River water was driven toward the east during sapropel S1 formation as it is in the present sea surface circulation. The most depleted $\delta^{18}O_{ruber}$ value in PS009PC (−1.26‰) is in line with the study of *Fontugne et al.* [1994] and confirms their statement that $\delta^{18}O_{ruber}$ is more depleted when compared to other eastern Mediterranean records [e.g., *De Lange et al.*, 2008] throughout the Holocene. Correspondingly, significantly more depleted $\delta^{18}O_{ruber}$ values were documented in the Israeli coastal area compared to the northern Levantine Basin (up to 1.3‰) during most of the Holocene [*Almogi-Labin et al.*, 2009]. These authors attribute this gradient mainly to Nile River water influencing the southeast Levantine Basin. This confirms that the Holocene $\delta^{18}O_{ruber}$ record from this location primarily reflects changes in isotopically light Nile discharge, which regulated local seawater $\delta^{18}O$ in this part of the Levantine Basin.

The general trends in our $\delta^{18}O_{ruber}$ record are similar to those observed in previously published archives of WAM [*Weldeab et al.*, 2007] and SIM [*Fleitmann et al.*, 2003] strength, supporting our hypothesis that $\delta^{18}O_{ruber}$ primarily reflects Nile discharge (Figures 4a, 4b, and 4d). These records show evidence for an increase in monsoon strength during the transition from the Younger Dryas to the Holocene Climatic Optimum. This is followed by a more gradual decline in monsoon strengths toward the late Holocene, which is likely a response to the gradual declining insolation at 30°N [*Fleitmann et al.*, 2003; *Laskar et al.*, 2004] (Figure 4c).

WAM peaked earlier (~11.3 cal kyr B.P.) than SIM strength (~9.4 cal kyr B.P.). Our $\delta^{18}O_{ruber}$ record also shows maximum Nile discharge close to 9.4 cal kyr B.P., suggesting the dominance of Indian Ocean-derived moisture on Nile discharge during the early to middle Holocene [see also *Hamann et al*., 2009].

The dominance of Indian Ocean moisture on Nile discharge during the early to middle Holocene seems to be related to the northerly position of the ITCZ, but this influence may have expressed itself in various ways. First, direct penetration of Indian Ocean air masses through the Ethiopian Highlands into the Blue Nile/Atbara watersheds may have been greater. This scenario is supported by generally more depleted $\delta^{18}O_{Nile}$ values during this time period [*Abell and Hoelzmann*, 2000; *Rodrigues et al*., 2000], as expected from moisture transported across the Ethiopian Highlands [*Kebede and Travi*, 2012]. Second, Lake Turkana was connected to the Nile via the Sobat River until ~5.3 cal kyr B.P. [*Garcin et al*., 2012]. Thus, at this time the land surface area with Indian Ocean influence to the Nile catchment was larger than today. Finally, prolonged, strong positive phases of the Indian Ocean Dipole [*Saji et al*., 1999] during the early to middle Holocene [*Abram et al*., 2007] may have increased the moisture transport from the Indian Ocean onto the African continent.

Considering the effect of direct penetration of Indian Ocean moisture through the Ethiopian Highlands, it should be noted that part of the depletion we observe in early to middle Holocene $\delta^{18}O_{ruber}$ may have related to variability in the oxygen isotopic composition of the Nile water itself ($\delta^{18}O_{Nile}$). The average $\delta^{18}O$ value of precipitation in the modern Nile catchment during August is approximately -1 to -2‰ (http://www.WaterIsotopes.org [e.g., *Bowen and Wilkinson* 2002]). However, values for cellulose-inferred oxygen isotopes of Lake Victoria [*Beuning et al*., 2002], for "fossil" water in aquifers in northwest Sudan [*Abell and Hoelzmann*, 2000] and for northwest Sudan shell material [*Rodrigues et al*., 2000], all show a relative depletion in oxygen isotope values of approximately -7 to -10‰ during the early to middle Holocene. Nevertheless, the clear coevolution of Ti/Al and $\delta^{18}O_{ruber}$ (see section 5.2) indicates that $\delta^{18}O_{ruber}$ was not just an expression of variability in changing precipitation sources affecting $\delta^{18}O_{Nile}$, but primarily of variability in the quantity of Nile discharge.

5.2. Inorganic Geochemical Proxies of Paleoenvironmental Conditions (Ti, Ba, and V)

Variability in Ti/Al has generally been interpreted as representing the relative contribution of aeolian input (high in Ti) in the eastern Mediterranean, especially for distal marine sediments [*Wehausen and Brumsack*, 2000; *Lourens et al*., 2001]. Nevertheless, sedimentary Ti/Al increases from west to east in the eastern Mediterranean, possibly due to an increase in material from Ti-rich basalts [*Wehausen and Brumsack*, 2000]. Today, approximately 97% of the main Nile sediment is derived from weathering of Miocene-Pliocene basalts in the Ethiopian Highlands and transported through the Blue Nile and Atbara Rivers to the eastern Mediterranean [*Foucault and Stanley*, 1989]. The Nile Ti/Al end-member (~0.19) has been observed to be even higher than that of Saharan dust (~0.11) [*Krom et al*., 1999]. Since the sediments in PS009PC are dominated by Nile material, the Ti/Al record likely reflects variability in contribution of White Nile versus Blue Nile/Atbara sediment and in particular weathering rates in the Ethiopian Highlands. These have been reported to increase during drier periods, due to reduced vegetation cover [*Krom et al*., 2002; *Box et al*., 2011]. Hence, the generally depleted Ti/Al values in our record observed during the African Humid Period (~11–5 cal kyr B.P.) are thought to represent reduced weathering in the Ethiopian Highlands at this time (Figure 4e). This concords well with the general trend of $\delta^{18}O_{ruber}$ (Figure 4d), implying that increased Nile discharge occurred simultaneously with decreased weathering in the Blue Nile catchment during the early to middle Holocene. Nevertheless, multicentennial variability is not well expressed in Ti/Al, which might indicate a buffered response of vegetation cover to precipitation in the Ethiopian Highlands on these time scales.

Three main barium sources may contribute to Ba concentrations in sediments, namely, biogenic barite ($BaSO_4$), Ba in aluminosilicates, and Ba associated with Mn/Fe oxides [e.g., *Schenau et al*., 2001]. Barium in the eastern Mediterranean has primarily been used as a proxy for paleo(export) productivity, showing generally a Ba (barite) enrichment during sapropel S1 deposition [e.g., *Thomson et al*., 1995; *Van Santvoort et al*., 1997; *Wehausen and Brumsack*, 1999; *Mercone et al*., 2000; *Jilbert et al*., 2010]. The Ba enrichment has been shown to be proportional to the initial organic carbon (C_{org}) accumulation rate during sapropel formation [*Van Santvoort et al*., 1997; *Thomson et al*., 1999; *De Lange et al*., 2008]. Hence, the Ba/Al enrichment during the S1 interval in PS009PC confirms that export productivity was enhanced in the Levantine Basin at this time (Figure 3d), showing a close correspondence to C_{org} (Figure 3c).

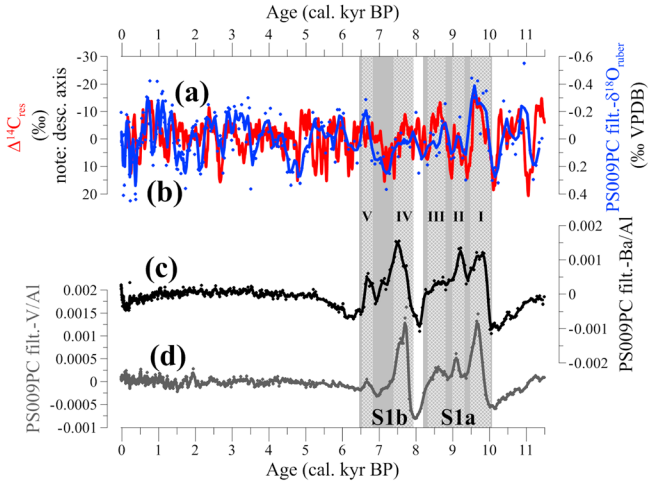

Figure 5. Comparison of (a) atmospheric $\Delta^{14}C_{res}$ used as proxy of solar variability (more negative values relate to increased solar activity) (red) [*Stuiver et al.*, 1998], (b) PS009PC $\delta^{18}O_{ruber}$ (blue), (c) PS009PC Ba/Al, and (d) PS009PC V/Al. PS009PC data have been detrended and notch filtered (see section 3.5). All data are three-point moving averages. Grey-shaded areas indicate period of sapropel S1 formation, while S1a and S1b are also specified. The periods of simultaneous relatively higher Ba/Al, higher V/Al, and more negative $\delta^{18}O_{ruber}$, during sapropel S1 formation, are marked I–V.

The redox sensitive element vanadium has been reported to be enriched in sediments deposited under reducing conditions, as in sapropels [e.g., *Thomson et al.*, 1995; *Nijenhuis et al.*, 1999; *Warning and Brumsack*, 2000; *Jilbert et al.*, 2010]. Generally, it has been observed that V is transformed from dissolved to solid species at specific redox potential thresholds at the sediment-water interface [*Emerson and Huested*, 1991]. The dissolution/precipitation of redox sensitive elements can be diagenetically redistributed through postdepositional oxidative alteration of these elements after reventilation of the water column [*Thomson et al.*, 1995]. This diagenetic oxygen penetration effect ("burn down") of sapropels is mainly dependent on sediment accumulation rates and less on bioturbation [*Van Santvoort et al.*, 1996]. For this core locality, being a very high sedimentation rate site (on average ~21 cm kyr^{-1}) compared to other eastern Mediterranean sites (2–3 cm kyr^{-1}), downward oxidation is negligible. Therefore, a relatively pristine vanadium distribution is observed which confirms that relatively reducing conditions were present throughout much of the S1 interval (Figure 3e).

5.3. Solar-Forced Multicentennial Variability in Nile Discharge

The multicentennial variability observed in our $\delta^{18}O_{ruber}$-derived Nile discharge record shows a strong resemblance to the atmospheric $\Delta^{14}C_{res}$ record throughout the Holocene (Figures 5a and 5b). A running correlation analysis of the two records confirms their similarity during the early to middle Holocene S1 interval (Figure 6b). A consistent positive correlation between PS009PC $\delta^{18}O_{ruber}$ and $\Delta^{14}C_{res}$ occurs during the early to middle Holocene, implying that Nile discharge increases when solar activity increases.

To assess the mechanisms of solar forcing on Nile discharge for these time scales, we also performed running correlation analyses between the $\Delta^{14}C_{res}$ record and the records of WAM and SIM strength (Figure 6b). The Oman $\delta^{18}O_{speleothem}$ has previously been interpreted to be influenced by solar forcing from ~8 cal kyr B.P. [*Fleitmann et al.*, 2003]. Our analysis shows that $\delta^{18}O_{speleothem}$ indeed displays temporally intermittent correlations with $\Delta^{14}C_{res}$ from ~8 cal kyr B.P. Meanwhile, the WAM record shows only occasional correlation with $\Delta^{14}C_{res}$ throughout the studied interval. The more prevalent solar signals in the SIM, relative to the WAM, record support our claim that Nile discharge was strongly influenced by Indian Ocean moisture during the early to middle Holocene. In addition, it indicates that solar-driven variability in Indian Ocean-derived moisture on multicentennial time scales dictated Nile discharge. However, it is surprising that the correlation between Nile discharge and solar output is so consistent, when the record of SIM strength shows only intermittent correlation to $\Delta^{14}C_{res}$. We suggest that our Nile discharge record faithfully represents solar forcing, while the Qunf Cave SIM record may be partly influenced by other factors dampening the solar signal. The Qunf $\delta^{18}O_{speleothem}$ record has been proposed to be influenced by Eurasian snow cover before ~8 cal kyr B.P. [*Fleitmann et al.*, 2003], which interfered with continent-ocean pressure gradients and potentially restricted the transmission of the monsoon onto the Arabian peninsula [*Barnett et al.*, 1988; *Overpeck et al.*, 1996].

The influence of solar variability on the Indian Ocean monsoon has been shown by studies of modern meteorological data sets [*Kodera*, 2004] and inferred from climate reconstructions of the Holocene [e.g., *Neff et al.*, 2001; *Gupta et al.*, 2005]. The solar influence is mainly expressed through stratospheric conditions, which

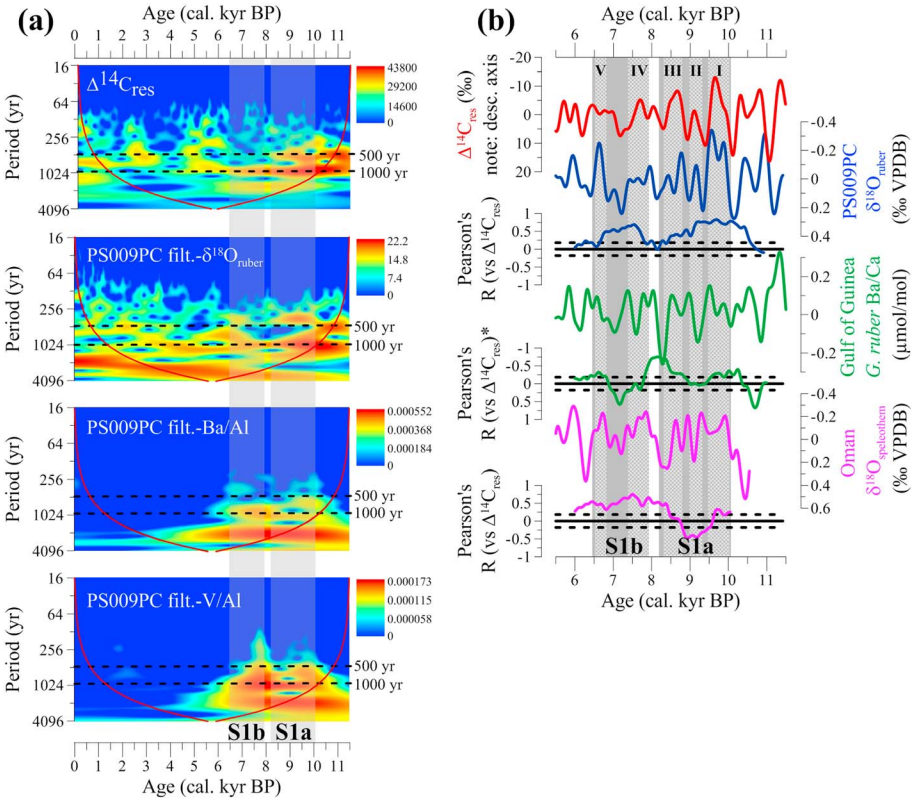

Figure 6. (a) Wavelet analyses of time series. Top to bottom: atmospheric $\Delta^{14}C_{res}$ relative to PS009PC $\delta^{18}O_{ruber}$, Ba/Al, and V/Al records (all detrended and notch filtered). See section 3.5 for further details on wavelet analysis. Black horizontal dashed lines mark periods of relatively strong power in $\Delta^{14}C_{res}$, $\delta^{18}O_{ruber}$, Ba/Al, and V/Al in the ~500 year to ~1000 year band (arbitrary). The cone of influence, under which boundary effects might become an issue [*Hammer et al.*, 2001], is indicated by solid red line in each wavelet. (b) Comparison of detrended and filtered data (0.256–3.333 kyr) of the time series. Top to bottom: Solar activity $\Delta^{14}C_{res}$ [*Stuiver et al.*, 1998], PS009PC $\delta^{18}O_{ruber}$ (this study), Gulf of Guinea *G. ruber* Ba/Ca [*Weldeab et al.*, 2007], and Oman $\delta^{18}O_{speleothem}$ [*Fleitmann et al.*, 2003]. Results of a running correlation are indicated in the same color (window width = 1005 year, shift increment = 5 year) of the "monsoon" time series to $\Delta^{14}C_{res}$. The 99% confidence threshold is indicated by black horizontal dashed lines (note that these are sensitive to the resampling). The asterisk indicates that the running correlation of the Gulf of Guinea *G. ruber* Ba/Ca has a reversed *y* axis; for this record a negative correlation indicates a high coherence between increased solar activity and increased monsoon activity. The periods of simultaneous higher Ba/Al, higher V/Al, and negative *G. ruber* oxygen isotope values, during sapropel S1 formation in core PS009PC, are marked I–V (based on Figure 5).

modulate equatorial tropospheric upwelling and thus the convective activity over the Indian Ocean sector [see *Kodera*, 2004; *Gupta et al.*, 2005]. Solar activity has been characterized by higher-amplitude variability in the interval ~11 to ~8 cal kyr B.P. than averagely observed during the Holocene [*Solanki et al.*, 2004]. Thus, the solar influence on Indian Ocean-derived precipitation in the Nile catchment (and hence Nile River discharge) may well have been larger during the early to middle Holocene.

5.4. Variable Nile Discharge and Sapropel S1 Formation

The start of sapropel S1 at ~10.1 cal kyr B.P. coincides with an increase of Nile discharge (shift to depleted $\delta^{18}O_{ruber}$, Figures 3a, 3c, and 3d) and with a shift to maximum activity of the SIM during the early Holocene [*Fleitmann et al.*, 2003] (Figure 4b). This correspondence may indicate that the increasing influence of Indian Ocean-derived moisture, transmitted through the River Nile, was an important final trigger for the onset of sapropel S1 formation [see also *Marino et al.*, 2009].

Furthermore, throughout S1, Nile discharge ($\delta^{18}O_{ruber}$) varies simultaneously on multicentennial time scales with (export) productivity (Ba/Al) and bottom water redox conditions (V/Al) (Figures 5b–5d). Five distinct intervals of increased Nile discharge, increased (export) productivity, and increased anoxia are observed at

~9.7, ~9.1, ~8.6, ~7.7, and ~6.6 cal kyr B.P. Wavelet analysis confirms that these three parameters also show similar spectra to that of $\Delta^{14}C_{res}$, with cyclicity in 500–1000 year band (Figure 6a). Hence, it appears that solar-driven variability in Nile discharge also controlled the intensity of sapropel formation in the southeast Levantine Basin on these time scales.

Increased Nile discharge may be expected to bring more nutrients to the Levantine Basin, increasing (export) productivity, thus also decreasing bottom water oxygen content through organic matter decay [*Rohling and Hilgen*, 1991; *De Lange et al*., 2008]. However, decreased ventilation (forced by an increased Nile outflow) would also decrease the bottom water oxygen content [*Rossignol-Strick et al*., 1982; *Rohling*, 1994; *De Lange et al*., 2008]. Core PS009PC is taken at a depth of 552 m, close to the lower boundary of the LIW today [*Schilman et al*., 2003]. The impact of Nile discharge on LIW formation has been indicated by modeling results which show that construction of the high Aswan Dam increased LIW formation by 30% due to the effect on salinity in the eastern Mediterranean [*Skliris and Lascaratos*, 2004]. Hence, periods of increased Nile discharge may have decreased LIW formation, and vice versa, influencing the residence time of water masses at the coring site. Nile discharge could, therefore, plausibly influence both productivity and ventilation on multicentennial time scales.

Solar forcing of ventilation of the eastern Mediterranean during S1 has been reported previously for a deep (3400 m water depth) Ionian site [*Jilbert et al*., 2010], implying that the influence of variable Nile discharge, and the underlying Indian Ocean monsoon influence, may have been more far reaching than the Levantine Basin alone. However, an interesting finding is the consistent coupling between export productivity (Ba/Al) and redox conditions (V/Al) on multicentennial time scales in PS009PC. Partial decoupling of these parameters, especially at very short (multidecadal) time scales, was observed by *Jilbert et al*. [2010] in the Ionian Sea. This contrast may be partly attributed to the differing controls on ventilation of the deep eastern Mediterranean with respect to the Levantine Basin. At deeper sites the hydrology of northern Mediterranean subbasins (and higher latitude climate) play an important role in controlling ventilation rates, through their influence on EMDW formation [*Rohling et al*., 2002; *Marino et al*., 2009; *Jilbert et al*., 2010], but do not necessarily regulate nutrient availability in the open eastern Mediterranean. Meanwhile, in the southeast Levantine Basin the Nile dominates both direct nutrient availability and ventilation through LIW formation.

The interruption in sapropel formation at ~8.1 cal kyr B.P. is distinct from the multicentennial variability marked I–V in Figure 5 and has been found before not only in this area [*Almogi-Labin et al*., 2009] but also in other eastern Mediterranean cores [e.g., *Casford et al*., 2003]. For this event, a relatively minor positive excursion in $\delta^{18}O_{ruber}$ is observed in core PS009PC, while variability in Ba/Al (and C_{org}) and V/Al are relatively large. Although Nile discharge was reduced, it seems not to be the main cause of this event. During this event surface water cooling has been observed in both Aegean and Adriatic Seas [*De Rijk et al*., 1999; *Rohling et al*., 2002]. Both basins are important for EMDW formation [*Schlitzer et al*., 1991; *Roether et al*., 1996]. This cooling event can tentatively be correlated to the well-studied ~8.2 kyr B.P. cooling event in the Northern Hemisphere [*Rohling and Pälike*, 2005]. In our data, Ba/Al remains relatively high compared to pre/post-S1 values, while C_{org} and V/Al show similar values to the pre/post-S1 intervals (Figures 3c–3e). This implies that export productivity remained relatively high during the interruption, while redox conditions became fully oxic, leading to efficient remineralization of newly deposited C_{org}. A rapid increase in ventilation seems the likeliest explanation for this anomalous event, possibly driven by severe winter cooling of SSTs in the northern part of the eastern Mediterranean [*Casford et al*., 2003]. This shows that the predominant control on variability within the sapropel in the study region is Nile discharge, but that this variability is also influenced by major contributions from northern climate regimes.

6. Conclusions

Our $\delta^{18}O_{ruber}$ record from a high sedimentation rate site in the southeast Levantine Basin may be one of the best records yet presented of Nile discharge during the early to late Holocene, showing significant variability in Nile discharge on (multi)centennial time scales. The early Holocene shift to maximum Nile discharge, at ~9.5 cal kyr B.P., correlates with the Southwest Indian summer monsoon record, which is fueled by Indian Ocean moisture. However, this does not correlate with the Atlantic Ocean-derived West African monsoon with its maximum at ~11.3 cal kyr B.P. This finding implies that during this time the Indian Ocean was the predominant moisture source for Nile outflow, whereas today the Atlantic Ocean is the main source. The

stronger influence of Indian Ocean-derived moisture made Nile discharge susceptible to solar-forced variability in Indian Ocean monsoon strength, leading to large variability in Nile discharge on multicentennial time scales. This variability in Nile discharge also influenced (export) productivity and redox conditions in the southeast Levantine Sea during the formation of sapropel S1, by modulating nutrient inputs and intermediate water ventilation.

Acknowledgments

We acknowledge the useful comments of Associate Editor David Lea and three anonymous reviewers, which were helpful to improve the manuscript. We thank Arnold van Dijk for analytical assistance with the foraminiferal oxygen isotope and total organic carbon measurements at the University of Utrecht. For the age model we acknowledge Piet van Gaever for ^{210}Pb analyses at the NIOZ and Tomasz Goslar for ^{14}C analyses at the Poznań Radiocarbon Laboratory. We thank Lucas Lourens of the University of Utrecht for help with notch filtering of the proxy records. The cores used in this study have been recovered during the PASSAP cruise with the R/V *Pelagia* in May 2000, as part of the PASS2-project funded by NWO. The captain, crew, and scientific participants are acknowledged for their onboard collaboration. Furthermore, Ahuva Almogi-Labin is acknowledged for discussion on the core site location. This paper is part of the PALM-project, funded by NWO. Data is made available upon request.

References

Abell, P. I., and P. Hoelzmann (2000), Holocene palaeoclimates in northwestern Sudan: Stable isotope studies on molluscs, *Global Planet. Change*, *26*, 1–12.

Abram, N. J., M. K. Gagan, Z. Y. Liu, W. S. Hantoro, M. T. McCulloch, and B. W. Suwargadi (2007), Seasonal characteristics of the Indian Ocean Dipole during the Holocene epoch, *Nature*, *445*, 299–302.

Almogi-Labin, A., M. Bar-Matthews, D. Shriki, E. Kolosovsky, M. Paterne, B. Schilman, A. Ayalon, Z. Aizenshtat, and A. Matthews (2009), Climatic variability during the last ~90 ka of the southern and northern Levantine Basin as evident from marine records and speleothems, *Quat. Sci. Rev.*, *28*, 2882–2896.

Barnett, T. P., L. Dumenil, U. Schlese, and E. Roeckner (1988), The effect of Eurasian snow cover on global climate, *Science*, *239*, 504–507.

Beuning, K. R. M., K. Kelts, J. Russell, and B. B. Wolfe (2002), Reassessment of Lake Victoria—Upper Nile River paleohydrology from oxygen isotope records of lake-sediment cellulose, *Geology*, *30*, 559–562.

Boaretto, E., H. K. Mienis, and D. Sivan (2010), Reservoir age based on pre-bomb shells from the intertidal zone along the coast of Israel, *Nucl. Instrum. Methods Phys. Res., Sect. B*, *268*, 966–968.

Boer, W., G. D. van den Bergh, H. de Haas, H. C. de Stigter, R. Gieles, and T. C. E. van Weering (2006), Validation of accumulation rates in Teluk Banten (Indonesia) from commonly applied 210Pb models, using the 1883 Krakatau tephra as time marker, *Mar. Geol.*, *227*, 263–277.

Bond, G. C., B. Kromer, J. Beer, R. Muscheler, M. N. Evans, W. Showers, S. Hoffmann, R. Lotti-Bond, I. Hajdas, and G. Bonani (2001), Persistent solar influence on North Atlantic climate during the Holocene, *Science*, *294*, 2130–2136.

Bowen, G. J., and B. Wilkinson (2002), Spatial distribution of delta O-18 in meteoric precipitation, *Geology*, *30*, 315–318.

Box, M. R., M. D. Krom, R. A. Cliff, M. Bar-Matthews, A. Almogi-Labin, A. Ayalon, and M. Paterne (2011), Response of the Nile and its catchment to millennial-scale climatic change since the LGM from Sr isotopes and major elements of East Mediterranean sediments, *Quat. Sci. Rev.*, *30*, 431–442.

Casford, J. S. L., E. J. Rohling, R. H. Abu-Zied, C. Fontanier, F. J. Jorissen, M. J. Leng, G. Schmiedl, and J. Thomson (2003), A dynamic concept for eastern Mediterranean circulation and oxygenation during sapropel formation, *Palaeogeogr. Palaeoclimatol. Palaeoecol.*, *190*, 103–119.

Castañeda, I. S., E. Schefuss, J. Patzold, J. S. Sinninghe Damsté, S. Weldeab, and S. Schouten (2010), Millennial-scale sea surface temperature changes in the eastern Mediterranean (Nile River Delta region) over the last 27,000 years, *Paleoceanography*, *25*, PA1208, doi:10.1029/2009PA001740.

Darbyshire, I., H. Lamb, and M. Umer (2003), Forest clearance and regrowth in northern Ethiopia during the last 3000 years, *Holocene*, *13*(4), 537–546.

De Lange, G. J., J. Thomson, A. Reitz, C. P. Slomp, M. Speranza Principato, E. Erba, and C. Corselli (2008), Synchronous basin-wide formation and redox-controlled preservation of a Mediterranean sapropel, *Nat. Geosci.*, *1*, 606–610.

De Rijk, S., A. Hayes, and E. J. Rohling (1999), Eastern Mediterranean sapropel S1 interruption: An expression of the onset of climatic deterioration around 7 ka BP, *Mar. Geol.*, *153*, 337–343.

Emerson, S. R., and S. S. Huested (1991), Ocean anoxia and the concentrations of molybdenum and vanadium in seawater, *Mar. Chem.*, *34*, 177–196.

Essallami, L., M. A. Sicre, N. Kallel, L. Labeyrie, and G. Siani (2007), Hydrological change in the Mediterranean Sea over the last 30,000 years, *Geochem. Geophys. Geosyst.*, *8*, Q07002, doi:10.1029/2007GC001587.

Fleitmann, D., S. J. Burns, M. Mudelsee, U. Neff, J. Kramers, A. Mangini, and A. Matter (2003), Holocene forcing of the Indian monsoon recorded in a stalagmite from Southern Oman, *Science*, *300*, 1737–1739.

Fontugne, M. R., and S. E. Calvert (1992), Late Pleistocene variability of the carbon isotopic composition of organic matter in the eastern Mediterranean: Monitor of changes in carbon sources and atmospheric CO2 concentrations, *Paleoceanography*, *7*(1), 1–20, doi:10.1029/91PA02674.

Fontugne, M., M. Arnold, L. Labeyrie, M. Paterne, S. E. Calvert, and J. C. Duplessy (1994), Paleoenvironment, sapropel chronology and Nile River discharge during the last 20,000 years as indicated by deep-sea sediment records in the eastern Mediterranean, in *Late Quaternary Chronology and Paleoclimates of the Eastern Mediterranean*, edited by O. Bar-Yosef and R. S. Kra, pp. 75–88, Radiocarbon, Tucson.

Foucault, A., and D. J. Stanley (1989), Late Quaternary paleoclimatic oscillations in East-Africa recorded by heavy minerals in the Nile delta, *Nature*, *339*, 44–46.

Garcin, Y., D. Melnick, M. R. Strecker, D. Olago, and J.-J. Tiercelin (2012), East African mid-Holocene wet–dry transition recorded in palaeo-shorelines of Lake Turkana, northern Kenya Rift, *Earth Planet. Sci. Lett.*, *331–332*, 322–334.

Gupta, A. K., M. Das, and D. M. Anderson (2005), Solar influence on the Indian summer monsoon during the Holocene, *Geophys. Res. Lett.*, *32*, L17703, doi:10.1029/2005GL022685.

Hamann, Y., W. Ehrmann, G. Schmiedl, S. Krüger, J. B. Stuut, and T. Kuhnt (2008), Sedimentation processes in the Eastern Mediterranean Sea during the Late Glacial and Holocene revealed by end-member modelling of the terrigenous fraction in marine sediments, *Mar. Geol.*, *248*, 97–114.

Hamann, Y., W. Ehrmann, G. Schmiedl, and T. Kuhnt (2009), Modern and late Quaternary clay mineral distribution in the area of the SE Mediterranean Sea, *Quat. Res.*, *71*, 453–464.

Hammer, Ø., D. A. T. Harper, and P. D. Ryan (2001), Past: Paleontological statistics software package for education and data analysis, *Palaeontol. Electron.*, *4*, 9.

Hecht, A., and I. Gertman (2001), Physical features of the eastern Mediterranean resulting from the integration of POEM data with Russian Mediterranean Cruises, *Deep Sea Res., Part I*, *48*, 1847–1876.

Hennekam, R., and G. De Lange (2012), X-ray fluorescence core scanning of wet marine sediments: Methods to improve quality and reproducibility of high-resolution paleoenvironmental records, *Limnol. Oceanogr. Methods*, *10*, 991–1003.

Jilbert, T., G. J. Reichart, P. Mason, and G. J. de Lange (2010), Short-time-scale variability in ventilation and export productivity during the formation of Mediterranean sapropel S1, *Paleoceanography*, *25*, PA4232, doi:10.1029/2010PA001955.

Kebede, S., and Y. Travi (2012), Origin of the δ^{18}O and δ^{2}H composition of meteoric waters in Ethiopia, *Quat. Int.*, *257*, 4–12.

Kodera, K. (2004), Solar influence on the Indian Ocean monsoon through dynamical processes, *Geophys. Res. Lett.*, *31*, L24209, doi:10.1029/2004GL020928.
Krom, M. D., R. A. Cliff, L. M. Eijsink, B. Herut, and R. Chester (1999), The characterisation of Saharan dusts and Nile particulate matter in surface sediments from the Levantine Basin using Sr isotopes, *Mar. Geol.*, *155*, 319–330.
Krom, M. D., J. D. Stanley, R. A. Cliff, and J. C. Woodward (2002), Nile River sediment fluctuations over the past 7000 yr and their key role in sapropel development, *Geology*, *30*, 71–74.
Lascaratos, A., R. G. Williams, and E. Tragou (1993), A mixed-layer study of the formation of Levantine Intermediate Water, *J. Geophys. Res.*, *98*(C8), 14,739–14,749, doi:10.1029/93JC00912.
Laskar, J., P. Robutel, F. Joutel, M. Gastineau, A. C. M. Correia, and B. Levrard (2004), A long-term numerical solution for the insolation quantities of the Earth, *Astron. Astrophys.*, *428*, 261–285.
Lourens, L. J., R. Wehausen, and H. J. Brumsack (2001), Geological constraints on tidal dissipation and dynamical ellipticity of the Earth over the past three million years, *Nature*, *409*, 1029–1033.
Marino, G., E. J. Rohling, F. Sangiorgi, A. Hayes, J. L. Casford, A. F. Lotter, M. Kucera, and H. Brinkhuis (2009), Early and middle Holocene in the Aegean Sea: Interplay between high and low latitude climate variability, *Quat. Sci. Rev.*, *28*, 3246–3262.
Mercone, D., J. Thomson, I. W. Croudace, G. Siani, M. Paterne, and S. Troelstra (2000), Duration of S1, the most recent sapropel in the eastern Mediterranean Sea, as indicated by accelerator mass spectrometry radiocarbon and geochemical evidence, *Paleoceanography*, *15*, 336–347, doi:10.1029/1999PA000397.
Mohamed, Y. A., B. J. J. M. van den Hurk, H. H. G. Savenije, and W. G. M. Bastiaanssen (2005), Hydroclimatology of the Nile: Results from a regional climate model, *Hydrol. Earth Syst. Sci.*, *9*, 263–278.
Neff, U., S. J. Burns, A. Mangini, M. Mudelsee, D. Fleitmann, and A. Matter (2001), Strong coherence between solar variability and the monsoon in Oman between 9 and 6 kyr ago, *Nature*, *411*, 290–293.
Nicholson, S. E. (2009), A revised picture of the structure of the "monsoon" and land ITCZ over West Africa, *Clim. Dyn.*, *32*, 1155–1171.
Nijenhuis, I. A., H. J. Bosch, J. S. S. Damste, H. J. Brumsack, and G. J. De Lange (1999), Organic matter and trace element rich sapropels and black shales: A geochemical comparison, *Earth Planet. Sci. Lett.*, *169*, 277–290.
Overpeck, J., D. Anderson, S. Trumbore, and W. Prell (1996), The southwest Indian monsoon over the last 18000 years, *Clim. Dyn.*, *12*, 213–225.
Paillard, D., L. Labeyrie, and P. Yiou (1996), Macintosh Program performs time-series analysis, *Eos Trans. AGU*, *77*(39), 379–379.
Pinardi, N., and E. Masetti (2000), Variability of the large scale general circulation of the Mediterranean Sea from observations and modelling: A review, *Palaeogeogr. Palaeoclimatol. Palaeoecol.*, *158*, 153–174.
Pujol, C., and C. V. Grazzini (1995), Distribution patterns of live planktic foraminifers as related to regional hydrography and productive systems of the Mediterranean Sea, *Mar. Micropaleontol.*, *25*, 187–217.
Ramsey, C. B. (2009), Bayesian analysis of radiocarbon dates, *Radiocarbon*, *51*(1), 337–360.
Reimer, P. J., and F. G. McCormac (2002), Marine radiocarbon reservoir corrections for the Mediterranean and Aegean Seas, *Radiocarbon*, *44*(1), 159–166.
Reimer, P. J., et al. (2009), Intcal09 and Marine09 radiocarbon age calibration curves, 0–50,000 years cal BP, *Radiocarbon*, *51*(4), 1111–1150.
Rodrigues, D., P. I. Abell, and S. Kropelin (2000), Seasonality in the early Holocene climate of Northwest Sudan: Interpretation of Etheria elliptica shell isotopic data, *Global Planet. Change*, *26*, 181–187.
Roether, W., B. B. Manca, B. Klein, D. Bregant, D. Georgopoulos, V. Beitzel, V. Kovačević, and A. Luchetta (1996), Recent changes in Eastern Mediterranean Deep Waters, *Science*, *271*, 333–335.
Rohling, E. J. (1994), Review and new aspects concerning the formation of eastern Mediterranean sapropels, *Mar. Geol.*, *122*, 1–28.
Rohling, E. J., and G. R. Bigg (1998), Paleosalinity and δ18O: A critical assessment, *J. Geophys. Res.*, *103*(C1), 1307–1318, doi:10.1029/97JC01047.
Rohling, E. J., and F. J. Hilgen (1991), The eastern Mediterranean climate at times of sapropel formation: A review, *Geol. Mijnbouw*, *70*, 253–264.
Rohling, E. J., and H. Pälike (2005), Centennial-scale climate cooling with a sudden cold event around 8,200 years ago, *Nature*, *434*, 975–979.
Rohling, E. J., P. A. Mayewski, R. H. Abu-Zied, J. S. L. Casford, and A. Hayes (2002), Holocene atmosphere–ocean interactions: Records from Greenland and the Aegean Sea, *Clim. Dyn.*, *18*, 587–593.
Rossignol-Strick, M., W. Nesteroff, P. Olive, and C. Vergnaud-Grazzini (1982), After the deluge: Mediterranean stagnation and sapropel formation, *Nature*, *295*, 105–110.
Saji, N. H., B. N. Goswami, P. N. Vinayachandran, and T. Yamagata (1999), A dipole mode in the tropical Indian Ocean, *Nature*, *401*, 360–363.
Schenau, S. J., M. A. Prins, G. J. De Lange, and C. Monnin (2001), Barium accumulation in the Arabian Sea: Controls on barite preservation in marine sediments, *Geochim. Cosmochim. Acta*, *65*, 1545–1556.
Schilman, B., M. Bar-Matthews, A. Almogi-Labin, and B. Luz (2001), Global climate instability reflected by Eastern Mediterranean marine records during the late Holocene, *Palaeogeogr. Palaeoclimatol. Palaeoecol.*, *176*, 157–176.
Schilman, B., A. Almogi-Labin, M. Bar-Matthews, and B. Luz (2003), Late Holocene productivity and hydrographic variability in the eastern Mediterranean inferred from benthic foraminiferal stable isotopes, *Paleoceanography*, *18*(3), 1064, doi:10.1029/2002PA000813.
Schlitzer, R., W. Roether, H. Oster, H. G. Junghans, M. Hausmann, H. Johannsen, and A. Michelato (1991), Chlorofluoromethane and oxygen in the Eastern Mediterranean, *Deep Sea Res. Part A*, *38*, 1531–1551.
Schmuker, B., and R. Schiebel (2002), Planktic foraminifers and hydrography of the eastern and northern Caribbean Sea, *Mar. Micropaleontol.*, *46*, 387–403.
Schnetger, B., H. J. Brumsack, H. Schale, J. Hinrichs, and L. Dittert (2000), Geochemical characteristics of deep-sea sediments from the Arabian Sea: A high-resolution study, *Deep Sea Res., Part II*, *47*, 2735–2768.
Siani, G., M. Paterne, E. Michel, R. Sulpizio, A. Sbrana, M. Arnold, and G. Haddad (2001), Mediterranean sea surface radiocarbon reservoir age changes since the Last Glacial Maximum, *Science*, *294*, 1917–1920.
Skliris, N., and A. Lascaratos (2004), Impacts of the Nile River damming on the thermohaline circulation and water mass characteristics of the Mediterranean Sea, *J. Mar. Syst.*, *52*, 121–143.
Solanki, S. K., I. G. Usoskin, B. Kromer, M. Schussler, and J. Beer (2004), Unusual activity of the Sun during recent decades compared to the previous 11,000 years, *Nature*, *431*, 1084–1087.
Stuiver, M., and T. F. Braziunas (1993), Sun, ocean, climate and atmospheric 14CO2: An evaluation of causal and spectral relationships, *Holocene*, *3*, 289–305.
Stuiver, M., P. J. Reimer, E. Bard, J. W. Beck, G. S. Burr, K. A. Hughen, B. Kromer, G. McCormac, J. Van der Plicht, and M. Spurk (1998), INTCAL98 radiocarbon age calibration, 24,000-0 cal BP, *Radiocarbon*, *40*(3), 1041–1083.
Thomson, J., N. C. Higgs, T. R. S. Wilson, I. W. Croudace, G. J. De Lange, and P. J. M. Van Santvoort (1995), Redistribution and geochemical behavior of redox-sensitive elements around S1, the most recent eastern Mediterranean sapropel, *Geochim. Cosmochim. Acta*, *59*, 3487–3501.

Thomson, J., D. Mercone, G. J. de Lange, and P. J. M. van Santvoort (1999), Review of recent advances in the interpretation of eastern Mediterranean sapropel S1 from geochemical evidence, *Mar. Geol.*, *153*, 77–89.

Tierney, J. E., S. C. Lewis, B. I. Cook, A. N. LeGrande, and G. A. Schmidt (2011), Model, proxy and isotopic perspectives on the East African Humid Period, *Earth Planet. Sci. Lett.*, *307*, 103–112.

Van Santvoort, P. J. M., G. J. De Lange, J. Thomson, H. Cussen, T. R. S. Wilson, M. D. Krom, and K. Ströhle (1996), Active post-depositional oxidation of the most recent sapropel (S1) in sediments of the eastern Mediterranean Sea, *Geochim. Cosmochim. Acta*, *60*, 4007–4024.

Van Santvoort, P. J. M., G. J. De Lange, C. G. Langereis, M. J. Dekkers, and M. Paterne (1997), Geochemical and paleomagnetic evidence for the occurrence of "missing" sapropels in eastern Mediterranean sediments, *Paleoceanography*, *12*, 773–786, doi:10.1029/97PA01351.

Wang, Y., H. Cheng, R. L. Edwards, Y. He, X. Kong, Z. An, J. Wu, M. J. Kelly, C. A. Dykoski, and X. Li (2005), The Holocene Asian monsoon: Links to solar changes and North Atlantic climate, *Science*, *308*, 854–857.

Warning, B., and H. J. Brumsack (2000), Trace metal signatures of eastern Mediterranean sapropels, *Palaeogeogr. Palaeoclimatol. Palaeoecol.*, *158*, 293–309.

Wehausen, R., and H. J. Brumsack (1999), Cyclic variations in the chemical composition of eastern Mediterranean Pliocene sediments: A key for understanding sapropel formation, *Mar. Geol.*, *153*, 161–176.

Wehausen, R., and H. J. Brumsack (2000), Chemical cycles in Pliocene sapropel-bearing and sapropel-barren eastern Mediterranean sediments, *Palaeogeogr. Palaeoclimatol. Palaeoecol.*, *158*, 325–352.

Weldeab, S., D. W. Lea, R. R. Schneider, and N. Andersen (2007), 155,000 years of West African monsoon and ocean thermal evolution, *Science*, *316*, 1303–1307.

Williams, M., M. Talbot, P. Aharon, Y. Abdl Salaam, F. Williams, and K. Inge Brendeland (2006), Abrupt return of the summer monsoon 15,000 years ago: New supporting evidence from the lower White Nile Valley and Lake Albert, *Quat. Sci. Rev.*, *25*, 2651–2665.

Wüst, G. (1961), On the vertical circulation of the Mediterranean Sea, *J. Geophys. Res.*, *66*, 3261–3271, doi:10.1029/JZ066i010p03261.